



ACADEMIE
DES SCIENCES
INSTITUT DE FRANCE

Comptes Rendus

Mécanique

Gaëtan Boissonneau, Andréa Tommasi, Fabrice Barou, Marco Antonio Lopez-Sánchez and Maurine Montagnat

Dynamic recrystallization and mechanical behavior of Mg alloy AZ31: Constraints from tensile tests with in-situ EBSD analysis

Volume 353 (2025), p. 235-258

Online since: 27 January 2025

<https://doi.org/10.5802/crmeca.267>

 This article is licensed under the
CREATIVE COMMONS ATTRIBUTION 4.0 INTERNATIONAL LICENSE.
<http://creativecommons.org/licenses/by/4.0/>



The Comptes Rendus. Mécanique are a member of the
Mersenne Center for open scientific publishing
www.centre-mersenne.org — e-ISSN : 1873-7234



Research article / Article de recherche

Dynamic recrystallization and mechanical behavior of Mg alloy AZ31: Constraints from tensile tests with in-situ EBSD analysis

Recristallisation dynamique et comportement mécanique de l'alliage de magnésium AZ31 : Contraintes issues d'essais de traction avec analyse EBSD in-situ

Gaëtan Boissonneau^{®,*,a}, Andréa Tommasi^{®,a}, Fabrice Barou^{®,a}, Marco Antonio Lopez-Sánchez^{®,b} and Maurine Montagnat^{®,c}

^a Geosciences Montpellier, CNRS, Université de Montpellier, France

^b Departamento de Geología, Universidad de Oviedo, Oviedo, Spain.

^c Univ. Grenoble Alpes, CNRS, IRD, G-INP, IGE, Grenoble, France

E-mails: gaetan.boissonneau@umontpellier.fr (G. Boissonneau),
andrea.tommasi@umontpellier.fr (A. Tommasi), fabrice.barou@umontpellier.fr
(F. Barou), lopezmarco@uniovi.es (M. A. Lopez-Sánchez),
maurine.montagnat@univ-grenoble-alpes.fr (M. Montagnat)

Abstract. We conducted tensile tests on Mg AZ31 samples with in-situ EBSD acquisition at 250°C and 10^{-3} s⁻¹ to characterize the evolution of dynamic recrystallization (DRX) and its effect on the mechanical behavior. To investigate the entire deformation range up to failure at 65–67% engineering strain, step-wise experiments were conducted with in-situ EBSD acquisition at 2–5% strain intervals. Both in-situ microstructural observations and statistical analysis of microstructural properties document continuous DRX with nucleation by association of bulging and subgrain rotation starting at strains as low as 6%. However, the microstructure evolves slowly, mainly by development of substructure (polygonization), with DRX limited to isolated clusters, until 35% strain. This long incubation period is followed by acceleration of DRX, with faster grain boundary migration allowing for development of a DRX-necklace structure, whose spatial heterogeneity controls the final strain localization at strains > 60%. The microstructural evolution contrasts with the bulk mechanical behavior, which displays a linear decrease in the hardening rate between 15 and 60% strain. Comparison of the observed texture evolution with predictions by polycrystal plasticity simulations without DRX shows that DRX-induced changes in texture counteract the geometrical hardening due to the texture evolution resulting from dislocation glide. Microstructural softening is, nevertheless, required to compensate for hardening due to increase in the dislocation density. The intensity of this softening has to steadily increase with strain to explain the decrease in hardening rate between 15% and 60% strain. The apparent discrepancy between the kinetics of the microstructural evolution and the mechanical behavior implies, however, that the bulk softening does not depend solely on the DRX volume fraction, but also on its spatial organization.

Résumé. Nous avons réalisé des essais de traction sur des échantillons de Mg AZ31 avec acquisition EBSD in situ à 250°C et 10⁻³ s⁻¹ pour caractériser l'évolution de la recristallisation dynamique (DRX) et son effet sur le comportement mécanique. Pour étudier toute la gamme de déformation jusqu'à la rupture à 65–67%

* Corresponding author

de déformation ingénierie, des expériences ont été menées avec une acquisition EBSD in situ à des intervalles de déformation de 2-5% et repolissage des échantillons à des intervalles de 15% de déformation. Les observations microstructurales in situ et statistique des propriétés microstructurales documentent une DRX continue avec germination par association de bulging et de rotation des sous-grains à partir de déformations aussi faibles que 6%. Cependant, la microstructure évolue lentement, principalement par le développement de sous-structure (polygonisation), avec une DRX se limitant à des amas isolés, jusqu'à une déformation de 35%. Cette longue période d'incubation est suivie d'une accélération de la DRX, avec une migration plus rapide des joints de grains permettant le développement d'une structure de DRX en collier, dont l'hétérogénéité spatiale contrôle la localisation finale de la déformation à des déformations > 60%. L'évolution microstructurale contraste avec le comportement mécanique global, qui montre une diminution linéaire du taux de durcissement entre 15 et 60% de déformation. La comparaison de l'évolution de la texture observée avec les prédictions par des simulations de plasticité polycristalline sans DRX montre que les changements de texture induits par DRX contrecarrent le durcissement géométrique dû à l'évolution de la texture résultant du glissement de dislocation. Un adoucissement microstructural est néanmoins nécessaire pour compenser le durcissement dû à l'augmentation de la densité de dislocation. L'intensité de cet adoucissement doit augmenter de façon continue avec la déformation pour expliquer la diminution du taux de durcissement entre 15% et 60% de déformation. L'écart apparent entre la cinétique de l'évolution microstructurale et le comportement mécanique implique cependant que l'adoucissement global ne dépend pas uniquement de la fraction volumique recristallisée, mais aussi de son organisation spatiale.

Keywords. Dynamic recrystallization, Mg alloy, quasi in-situ EBSD, texture.

Mots-clés. Recristallisation dynamique, alliage Mg, EBSD quasi in-situ, texture.

Funding. This work was supported by the European Research Council (ERC) under the European Union Horizon 2020 Research and Innovation program [grant agreement No 882450 - ERC RhEoVOLUTION].

Electronic supplementary material. Supplementary material for this article is supplied as a separate archive available from the journal's website under article's URL or from the author.

Manuscript received 13 June 2024, revised 28 August 2024, accepted 5 September 2024.

1. Introduction

Dynamic recrystallization (DRX) shapes the mechanical properties of polycrystalline materials during deformation at high temperature. It produces bulk softening by a series of mechanisms active at the grain and lower scales cf. reviews [1–3]. Local grain-to-grain viscoplastic strain incompatibility produces elastic strains that lead to stress concentrations. These stress concentrations may be relaxed by DRX via nucleation by grain boundary migration (bulging), polygonization (formation and evolution of low angle boundaries by absorption of dislocations resulting in progressive misorientation of adjacent grain volumes), or combination of both. The newly formed grains then grow as a function of the local gradients in dislocation density and the energy and properties of grain boundaries. Depending on the initial grain size and deformation conditions (temperature and strain rate), DRX leads to either grain refinement or coarsening (e.g., [4] for Mg alloys). DRX also impacts the texture evolution as the DRX grains, being formed in regions with high dislocation densities, often display a significant misorientation relative to the mean orientation of the parent grain, and by selective growth of grains in lower energy orientations [1, 2]. Thus, DRX changes the mechanical behavior via its effect on both the polycrystal microstructure (dislocations and grain boundary structure) and texture [5]. However, the local nature of the DRX mechanisms still hinders the establishment of clear relations describing the impact of DRX on the mean properties of a polycrystal.

In this study, we investigate the microstructure and texture evolution during DRX in Mg alloys AZ31 (Mg-3Al-1Zn) deformed under uniaxial tensile loading by means of quasi in-situ Electron Backscatter Diffraction (EBSD) monitoring. Mg alloys present a strong industrial interest owing, mainly, to their low density and high specific strength (see e.g. [6, 7]). They are also good analogs

for materials for which experiments using in-situ EBSD monitoring are not possible, like ice [8–10] or rocks [11, 12]. Mg has an hexagonal close-packed (hcp) crystallographic structure and few slip modes to accommodate deformation along the c-axis of the unit cell, in particular at low temperature. This viscoplastic anisotropy results in low ambient temperature formability. At high temperature, the viscoplastic anisotropy is reduced and the formability enhanced [13]. High temperatures also favor dynamic recrystallization (e.g. [7, 14–16]). In AZ31, DRX operates from 100°C to 450°C (e.g. [14, 17]). Recrystallization mechanisms can be divided, according to the nature of the recrystallization process, into two main groups: continuous and discontinuous recrystallization. Continuous DRX (CDRX) proceeds by continuous absorption of dislocations in subgrain boundaries (low angle boundaries), which eventually results in the formation of high angle boundaries and thus, new grains (see e.g.[18, 19]). Discontinuous recrystallization (DDRX) involves the nucleation of new grains mainly by bulging, typically at pre-existing grain boundaries, followed by growth (see e.g.[14, 17, 20]). Depending on the material composition and microstructural characteristics, DDRX and CDRX may coexist over a wide range of temperatures and strain rates [21]. Twinning-assisted DRX, where twins are favored nucleation sites, is also frequently observed, in particular at low temperature (see e.g. [14, 22–24]). Microstructure evolution during DRX in AZ31 is often characterized by the formation of a necklace of small grains surrounding initial larger grains [4, 14, 17], in particular when grain boundary serration and nucleation by bulging are favored. In classical necklace models, as described in [25], the nucleation progresses from the grain boundaries towards the core, up to recrystallization of the entire volume. However, the succession of mechanisms responsible for the necklace formation and growth or the separation between continuous and discontinuous DRX are insufficiently constrained by post-mortem observations [24, 26].

The tensile tests with quasi in-situ Electron Backscatter Diffraction (EBSD) monitoring of the microstructure evolution on AZ31 Mg alloy samples presented in this study combine: (1) local observations of the physical processes involved in DRX, (2) quantitative analysis of the microstructure changes at the polycrystal scale, and (3) the evolution of the mechanical behavior with increasing strain. We analyse the relations between the mechanical and bulk microstructural data (intragranular misorientation, grain size and recrystallized fraction) and document the different processes involved in DRX based on sequential crystal orientation maps mapped over a large strain range, up to 67% engineering strain, at strain rates and temperature conditions selected to maximize DRX. We also constrain the relative contributions of DRX-induced microstructural and textural evolution to the mechanical behavior by comparing the observed texture with predictions of viscoplastic self-consistent simulations.

2. Method

2.1. Starting material

Bone-shaped tensile samples (see Supplementary Material, Figure S1) were cut from a cylindrical rod of commercially pure hot-extruded AZ31 magnesium alloy by electric discharge machining at 30–35° to the initial extrusion direction. This results in a strong initial texture characterized by a girdle of $\langle c \rangle$ axis at 55–60° to the tension axis, which favors basal glide and inhibits twinning during the experiments. The assumption of minimal activity of twinning systems is verified a posteriori by the quantification of twin grain boundary fractions in the EBSD data (see Supplementary Material, Table T1).

Before deformation, the samples were annealed at 400°C for 24 hours and polished with: #2400 and #4000 mesh grits, 6, 3, and 1 µm oil-based diamond suspensions and Oxide Polishing Suspension (OPS). Ultrasonic ethanol baths were used to clean the surface between the different polishing steps and before EBSD analysis.

2.2. In-situ tensile testing

Tensile tests were conducted inside the CamScan X500-FE CrystalProbe scanning electron microscope (SEM) chamber using a NewTec Scientific MT1000 high temperature tensile rig. Samples were heated to 250 °C ($T/T_f = 0.58$) and deformed at a constant velocity of $7 \mu\text{m s}^{-1}$, which results in initial strain rates of 10^{-3} s^{-1} . These experimental conditions correspond to a Zener-Holomon parameter $Z = 3 \times 10^{10} \text{ s}^{-1}$ assuming an activation energy $Q = 135 \text{ kJ mol}^{-1}$ [27]. The temperature is controlled using thermocouples located under the sample heads and in the center of the gauge section. Engineering strains are calculated based on a 7 mm initial length. Stress data are corrected for the reduction in section with increasing strain by assuming conservation of volume and uniform deformation of the sample.

The deformation was halted at engineering strain intervals varying between 2 to 5% for EBSD mapping. Interruption of deformation disturbs the macroscopic mechanical response of the specimens (cf. Section 3.1). Two strategies were used to minimize this perturbation: (i) holding the sample at 250°C, which results in stress relaxation during the EBSD acquisition, or (ii) rapidly cooling the sample to 150°C upon reaching the target strain and keeping it at 150°C during EBSD acquisition, which produces a stress peak due to thermal contraction.

Out-of-plane deformation during the experiment reduces the indexing rate of EBSD maps, particularly around grain boundaries and triple junctions, where dynamic recrystallization is expected to occur. By adjusting the averaging parameter of the Kikuchi pattern acquisition, i.e. increasing the number of Kikuchi patterns acquired for each datapoint, we were able to obtain high quality EBSD maps for up to 15-20% accumulated engineering strain without repolishing. To map recrystallization processes at larger strains, samples were repolished at 15% strain intervals. Some samples were pre-deformed outside the SEM up to multiple engineering strains of 10 to 35% (Figure 1). The addition of the in-situ observations for 12 experiences covering 15-20% strain intervals on 6 samples produced a continuous dataset up to an engineering strain of 67% (Figure 1). In addition, one sample (H) was deformed ex-situ using the same rig and similar conditions to provide a reference for the mechanical behavior and final microstructure observations.

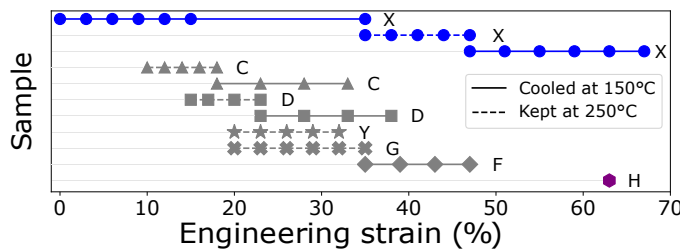


Figure 1. Experimental dataset: each line represents a continuous experiment with in-situ EBSD maps (symbols) acquired without repolishing the sample. Sample H was deformed without in-situ EBSD acquisition and is used as a reference for the mechanical data.

2.3. EBSD acquisition and post-processing

Crystal orientation maps were acquired by indexation of EBSD patterns on a fixed small domain in the central part of the sample. In addition, at the end of each experiment, EBSD mapping was performed over larger areas after repolishing the samples. Acquisition step size ranges from 0.5

μm for the small maps to $2 \mu\text{m}$ for the larger maps. The detailed acquisition conditions, areas, and step sizes for all EBSD maps are summarized in Supplementary Materials, Table T1.

The EBSD data were treated and analyzed using the open-source MTEX MATLAB toolbox v5.6.1 (<https://github.com/mtex-toolbox/mtex>). Measurements with a mean angular deviation higher than 1.3° were neglected. Grain boundaries were identified using a 7.5° misorientation threshold and smoothed (two iterations). Grains defined by less than four pixels were removed from the dataset. EBSD data were smoothed using a half-quadratic filter within each grain. We imaged and quantified the evolution of the microstructure based on: (1) the intragranular misorientation, (2) the subgrain ($\text{low angle} < 7.5^\circ$) boundary and grain boundary densities, (3) the grain sizes, and (4) the recrystallized fraction. The intragranular misorientation produced by the accumulation of geometrically necessary dislocations (GND) was estimated based on: (1) the kernel average misorientation (KAM), which is the average value of the misorientation between a pixel and its neighbors, (2) the grain orientation spread (GOS), which is the mean deviation of the local orientations relative to the mean orientation of the grain, and (3) the local misorientation (axis and intensity) to the mean orientation of the grain (mis2mean). KAM and mis2mean maps were used to document subgrain boundaries and subgrains within a grain, respectively. First order KAM data was used if not specified otherwise. For comparing KAM data over the entire dataset, the higher resolution EBSD maps were downsampled to match the coarser step size ($2 \mu\text{m}$). Subgrain and grain boundary densities were estimated as the ratio of the total length of subgrain or grain boundaries relative to the map area. Grain size was quantified by the diameter of a circle with the same area as the grain (i.e. equivalent diameter).

Recrystallized grains were discriminated based on either a GOS or a grain size threshold. The first criteria is based on the assumption that recrystallization cleans the dislocation substructure. It highlights recently nucleated grains, in particular those formed by bulging [4]. It does not keep track of DRX grains in which intragranular misorientation increases due to deformation, nor of DRX grains formed by polygonization, which may create DRX nuclei with a non-negligible misorientation. In the first deformation steps, the GOS threshold also includes statically recrystallized grains produced by the pre-deformation annealing in the RX population. On the other hand, identification of DRX grains based on a grain size threshold, which is commonly used in absence of orientation data (e.g. [28]), is biased by the 2D sectioning. One may avoid this bias by focusing on the evolution of such data with strain and not on the absolute values. The grain size threshold includes DRX grains formed by both bulging and polygonization, but keeps no memory of fast-growing RX grains; the evolution of the DRX fraction defined based on a grain size threshold depends therefore also on the grain growth rate. Analyzing the DRX fraction defined by the two thresholds separately allows therefore to characterize different aspects of the DRX process. In the present study, the absolute values of the two thresholds were chosen empirically. In the main text, we present results for a GOS threshold of 1° or an equivalent diameter of $20 \mu\text{m}$, based on the analysis of the KAM maps and grain size distributions. Different grain size and GOS threshold values result in different absolute values for the recrystallized fraction at a given deformation step, but define similar evolution trends (see Supplementary Materials Figure S2).

2.4. Texture evolution analysis

To quantify the effect of DRX on the texture evolution, we compare the textures measured at different strains to that predicted for a monotonic uniaxial tension test by a viscoplastic self-consistent model (VPSC) [29] with no recrystallization. The simulations were performed using the VPSC7 code [30] with a 2nd order linearization procedure [31], with a normalization factor equal to 1, a stress exponent of 7 [32], and CRSS in the range of those typically used for modelling deformation of AZ31 at high temperature and moderate strain rates [13, 33]. Boundary conditions

mimic the experimental ones by imposing a fixed rate extension in the direction 1, null normal stresses in directions 2 and 3, and null shear velocity gradients.

To allow estimating how DRX modified the geometrical (texture-induced) component of hardening, hardening due to dislocations interactions was not considered in the present VPSC simulations. The effect of DRX on the geometrical hardening is estimated by comparing (1) the stresses predicted for a monotonic axial tension VPSC simulation using as the initial texture that measured for the starting material to (2) those predicted by one-step VPSC simulations run with the same parameters, but using as the initial texture those measured in the experiments at different strains.

The reference simulation, presented in the main text, has critical resolved shear stresses (CRSS) for the basal $\langle a \rangle$, prismatic $\langle a \rangle$, and pyramidal $\langle a+c \rangle$ systems of 3, 40, and 40 MPa and 40 and 130 MPa for tension $\{10\bar{1}2\}\langle\bar{1}011\rangle$ and compression $\{10\bar{1}1\}\langle\bar{1}012\rangle$ twinning. These CRSS are based on data obtained by Chapuis and Liu [33] by adjusting experiments on AZ31 at 250°C and 10^{-2} s⁻¹. Since the texture evolution and the associated geometrical hardening depend on the imposed viscoplastic anisotropy (contrast between the CRSS of the basal and other systems) and the strain-rate sensitivity, additional simulations with higher and lower viscoplastic anisotropy and a stress exponent of 10 are presented in the Supplementary Material.

2.5. Limitations of the experimental setting

Interruption of the deformation for in-situ acquisition of the EBSD data perturbs the macroscopic stress-strain response. Reducing the temperature to 150°C produces thermal stresses in the sample. Keeping the sample at 250°C during the mapping results in partial annealing of the sample and stress relaxation in the assemblage. To minimize annealing, the in-situ EBSD acquisition time had to be limited. By consequence, a compromise was made on the size of the in-situ EBSD maps, which are too small to be representative volume elements. To estimate the representativity of the in-situ EBSD data, maps over larger areas were acquired post-mortem for most samples. The large number of EBSD maps acquired in the present study (see Supplementary Materials table T1) further ensures the statistical representativity of the microstructural variables derived from the EBSD maps.

EBSD providing a two-dimensional description of the microstructure at the sample surface, growth of grain nuclei out of the observation plane cannot be discriminated from nucleation on the plane. Due to the deterioration of the surface, acquisition of data on a constant area is limited to 15-20% cumulative strain before the sample has to be re-polished. However, the data presented in Section 3.3 show that this strain interval is sufficient to document the local DRX evolution. The analysis of multiple tests with overlapping strain intervals allows to verify the reproducibility of the observations. The comparison between interrupted tests and the continuous one performed out of the SEM (sample H) is used to evaluate the impact of the specific conditions used for EBSD monitoring on the mechanical response and microstructure evolution.

3. Results

3.1. Bulk mechanical behavior

All experiments display a consistent mechanical behavior illustrated by the true stress/engineering strain curves for the two samples deformed up to the highest strain (Figure 2). Sample H (purple curve in Figure 2) was deformed outside the SEM without interruption until failure to be used as a reference. The true stress/engineering strain curve displays an elastic loading phase

of up to 2% strain, followed by strain hardening. The hardening rate decreases markedly at 10–15% engineering strain. This is followed by a constantly decreasing hardening rate, which leads to a smooth transition from hardening to softening at ~30% engineering strain, and accelerated softening for engineering strains > 60%, with ductile failure at 63% strain.

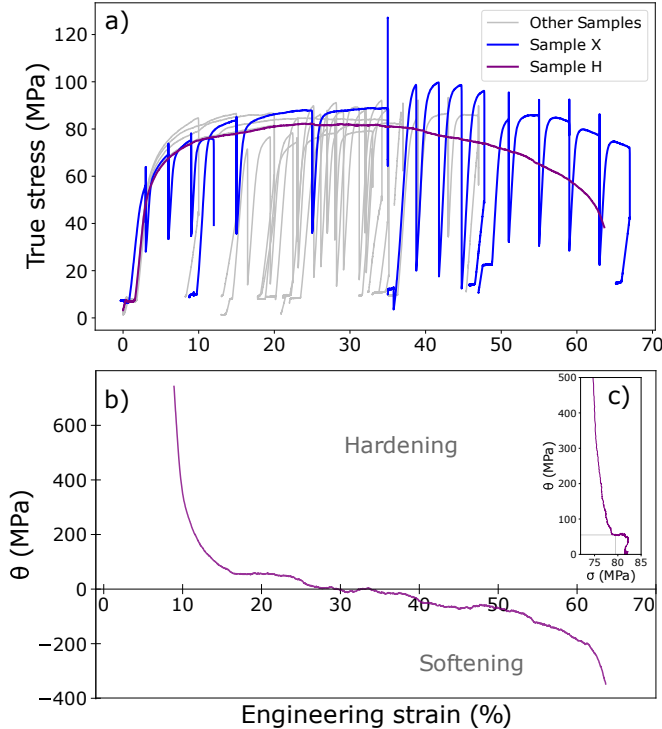


Figure 2. **a)** True stress/engineering strain curves for all tests. Data for samples X and H, which cover the full strain range and are discussed in detail in the text, are highlighted in blue and purple, respectively. Sample H was deformed without in-situ EBSD acquisition and is used as a reference. **b)** Evolution of the work hardening/softening rate ($\theta = d\sigma/d\varepsilon$) with strain, described by the first derivative of the true stress/engineering strain curves of Sample H. To mitigate the experimental noise, θ was calculated from raw data as the slope between each data point and the point $\sim 0.6\%$ strain ahead. **c)** Work hardening rate function of the true stress (σ) for sample H. The inflection is identified for a critical stress σ_c of 79.5 MPa, corresponding to a critical strain ε_c of 18%.

The behavior of Sample X (blue curve in Figure 2) is representative of the mechanical response of the experiments in which the deformation was halted for in-situ EBSD mapping. Each interruption induced a stress relaxation, manifested as a vertical drop in the stress/strain curve. Resumption of the deformation resulted in elastic reloading of the samples over at least 1% strain. This resulted in “stretching” of the mechanical curves of the in-situ experiments relative to that of sample H. Three distinct deformation experiments (0% to 35%; 35% to 47%; 47% to 67%) were performed sequentially on this sample, with unloading and repolishing of the sample surface between the experiments. The true stress/engineering strain curves of the three experiments were assembled to construct the curve shown by the blue line in Figure 2. The stress relaxation at 10% strain is a consequence of a reboot of the tensile rig software due to a technical issue. The

two strategies for EBSD acquisition presented in Section 2.2 have been tried on this sample: the segments of the curve displayed with full lines in Figure 1 present data for EBSD acquisition at 150°C, whereas those displayed as dashed lines show the data for EBSD acquisition at 250°C. The stress peak at 35% strain for sample X is a consequence of thermal contraction of the sample as it was cooled down to room temperature. This might have caused some hardening and explain the 10 MPa offset of the mechanical data for strains > 35%. For the other experiments, unloading and cooling were synchronized to avoid such stress peaks.

In summary, despite small perturbations due to halting of the tensile load for EBSD acquisition, the mechanical behavior of the samples with in-situ EBSD acquisition is consistent with that of sample H. The observed stress-strain curves are similar to those described by Tam et al. [26] for tensile tests at on Mg AZ31 at 200°C. Optical inspection of the evolution of the samples shape with increasing strain do not document any progressive necking. Deformation is rather homogeneous until catastrophic development of a semi-brittle shear band close to the end of the experiment, at engineering strain > 60%. (see Figure 3).

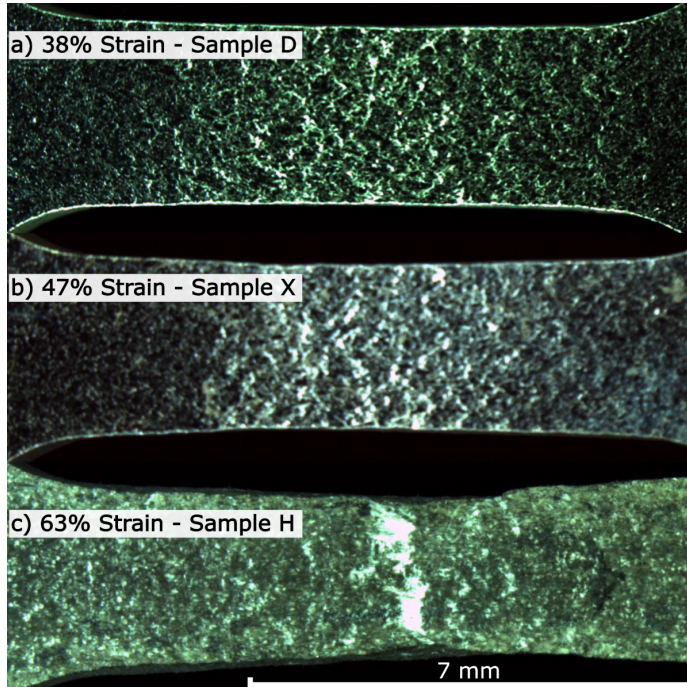


Figure 3. Optical images of the gauge area of three samples at increasingly high engineering strains. **a)** Sample D, 38% engineering strain. **b)** Sample X, 47% engineering strain. **c)** Sample H, 63% engineering strain.

3.2. Bulk microstructural analysis

The microstructural evolution across the entire strain range sampled in the present experiments is illustrated in Figure 4 by misorientation maps obtained post-mortem over large areas on different experiments (see Section 2).

The microstructure evolves from an initial state characterized by coarse grains with curved grain boundaries and almost free of substructure (GNDs) interspersed with aggregates of smaller

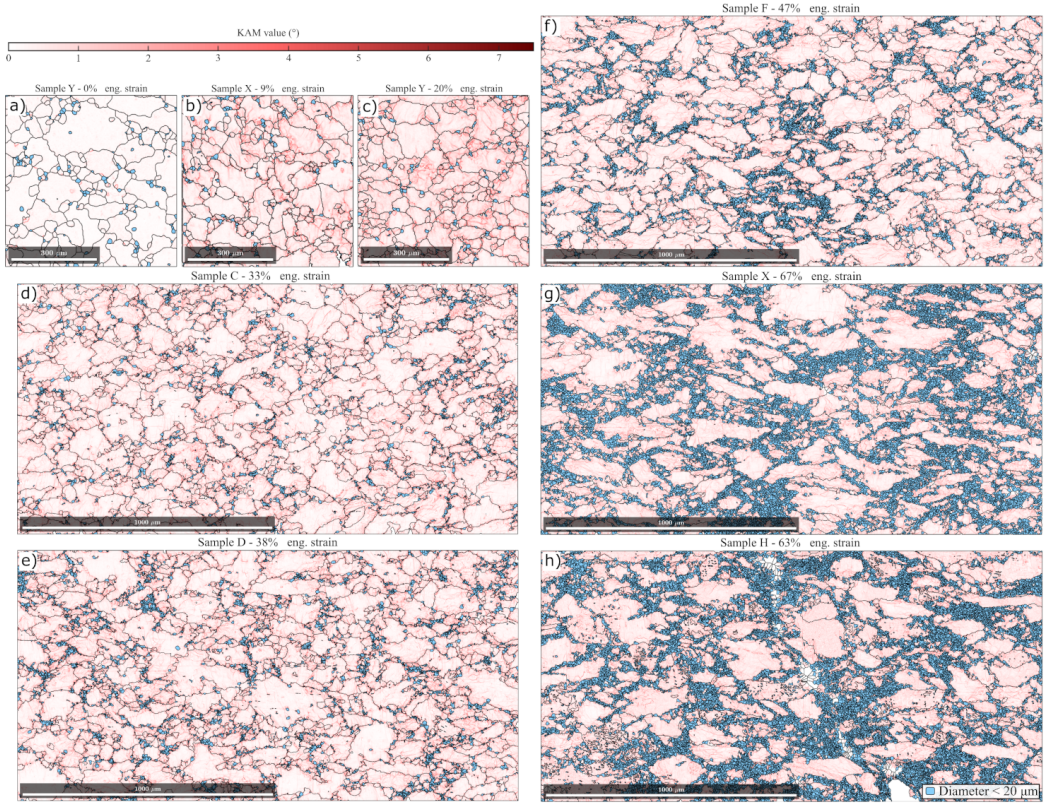


Figure 4. Overview of the microstructure evolution with increasing strain based on observations across multiple samples. **a)** Sample Y, undeformed. **b)** Sample X deformed to 9% engineering strain. **c)** Sample Y deformed to 20% engineering strain. **d)** Sample C deformed to 33% engineering strain. **e)** Sample D deformed to 38% engineering strain. **f)** Sample F deformed to 47% engineering strain. **g)** Sample X deformed to 67% engineering strain. **h)** Sample H deformed to 63% engineering strain, the low indexation domain that crosscut the sample materialises the final ductile failure plane. Grain boundaries defined based on a 7.5° misorientation threshold are represented as black lines. Recrystallized grains identified using an equivalent diameter of 20 μm threshold are coloured in blue. Data displayed in panels a), b), c) have been acquired with a 2 μm step size, in panel e) with a 1.5 μm step size, in panels d), f), g) and h) with a 1 μm step size.

polygonal grains, toward, at the highest strains, a necklace structure, characterized by a quasi-continuous network of very fine grains enclosing variably elongated and strongly deformed coarse grains. With increasing strain, the coarse grains become progressively more elongated, but maintain irregular shapes. They progressively develop a substructure and their grain boundaries became more serrated. Up to 33% strain, DRX events are irregularly distributed within the sample, leading to formation of isolated DRX grains or small clusters of DRX grains along the boundaries of coarse grains and triple junctions. At 38% strain (Figure 4(e)), the clusters of DRX grains have increased in size and number, leading to a clearly bimodal grain size distribution, but they are still isolated. At 47% strain, the DRX clusters start to interconnect at a scale of a few coarse grains. However, is only at the largest strain values, > 60%, that a necklace structure develops. At this stage, the DRX clusters have significantly increased in area and most coarse grain boundaries

are lined by DRX grains. This results in interconnection between DRX clusters at the sample scale and formation of a network of fine grained bands with irregular shapes, dominantly oriented at 25 to 45° to the tension direction. In sample H, deformed outside the SEM until ductile failure, the failure zone, which is oriented at ca. 60° to the tension direction seems to have formed by coalescence of the more developed of these bands. However, even at the highest strains, the coarse grains still compose > 70% of the sample area and they are not systematically surrounded by a necklace of small grains. Moreover, although the DRX clusters increased in area, they mainly extended laterally to form an interconnected network, with limited progression of DRX towards the interior of the coarse grains.

Dislocation substructures (and the associated GND density) accumulate up to about 40% strain, after which they stabilize. This evolution is quantified by the KAM distributions in both in-situ and post-mortem EBSD maps (Figure 5(a)). The median KAM displays a steady but slow increase and the KAM distribution becomes progressively more skewed, indicating increase in misorientation across subgrain (low angle) boundaries up to 40% strain. All KAM values were calculated using a homogeneous resolution of 2 μm . The variability in the measurements is to be attributed to sampling bias, due to variations in the mapped area (represented by the grey level scale for the 2nd and 3rd quartiles), as well as to spatial variability in the microstructure at the sample scale.

The subgrain (low angle) boundary density displays a similar evolution to that of the KAM values (Figure 5(c)), characterized by a linear increase as a function of strain up to ca. 40% strain and stabilization thereafter. As for the KAM values, dispersion among data for similar strains may be attributed to sampling bias. In particular the significant difference in subgrain boundary densities between the in-situ and post-mortem EBSD maps for the two most strained samples results from focusing the in-situ mapping in the most strained area of the sample, whereas the large-scale post-mortem EBSD data cover also less strained domains far from the necking region (see Figure 4). The grain (high angle) boundary density shows a markedly different evolution to the subgrain boundary density. It remains stable up to ca. 35% strain and steadily increases thereafter (Figure 5(d)).

The grain-size distribution (Figure 5(b)) remains highly bimodal over the entire strain range although the number and area-fraction occupied by small grains increases with strain (Figure 5(f)). All parameters describing the grain size distribution (median, first and third quartiles, and maximum excluding outliers in Figure 5(b)) remain almost constant up to about 35% strain. Median equivalent diameters decrease abruptly from > 20 μm to ~ 7 μm afterwards. Third quartiles and maxima show an even more marked decrease. This evolution is paired with the initiation of the development of a necklace-type microstructure of fine DRX grains surrounding coarse deformed grains, marked by a progressive increase in the number and size of the clusters of small grains (Figures 4(g-h)).

The RX fraction is analysed by means of two threshold parameters, a 1° GOS threshold and < 20 μm equivalent diameter threshold (see section 2.3). For both criteria (Figures 5(e-f)), we observe a transition at about 35% strain, with a progressive increase in the grain-size-based RX fraction up to ca. 25% and a more discontinuous increase in the GOS-based RX fraction up to ca. 12-15%. The error bars for the data derived from the larger post-mortem EBSD maps in Figures 5(e-f) provide an estimation of the variability expected for the measurements on maps with areas too small to be representative. These error bars have been calculated by sub-dividing the large maps into smaller areas, with similar dimensions to that of the in-situ EBSD maps.

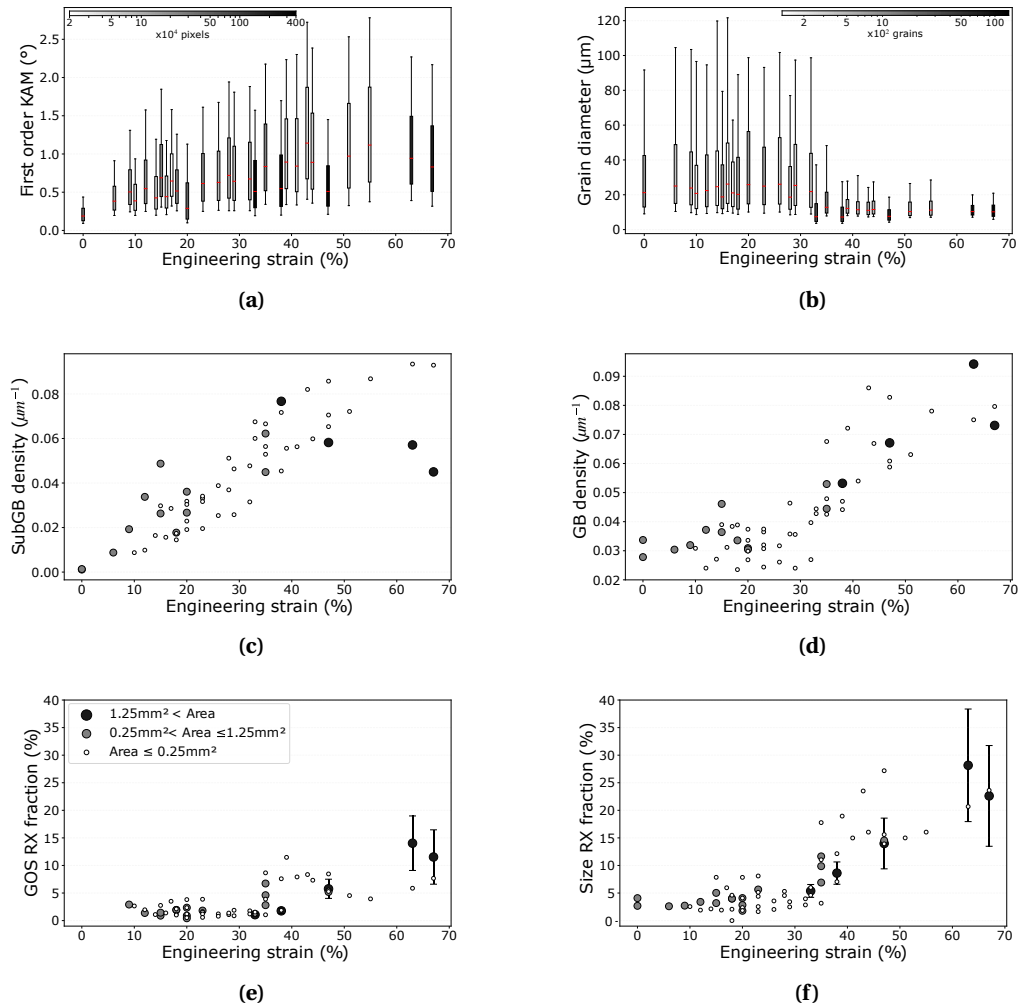


Figure 5. Evolution with the engineering strain of (a) the intragranular misorientation defined by the 1st order Kernel Average Misorientation (KAM), (b) the grain size distributions, (c) the subgrain (misorientation angle $< 7.5^{\circ}$) boundary density, (d) the grain boundary (misorientation angle $> 7.5^{\circ}$) density, and the recrystallized area fraction based on (e) a 1° GOS threshold and (f) a 20 μm equivalent diameter threshold. Data from multiple EBSD maps on a single or multiple samples at similar engineering strains were concatenated to increase the statistics. In a) and b), the boxes define the first and third quartiles, the median is highlighted in red, and the extremes bounds of the whiskers represent the 10th and 90th percentiles of the data. The box color is function of the number of data points in each distribution, with darker colors marking the data with large sample sizes (graphic legends on the top of each plot). In the RX fraction based on the GOS threshold plot (panel e) data for strains $< 9\%$ is not represented because this criterion does not discriminates between statically and dynamically RX grains.

3.3. Recrystallization mechanisms

Analysis of the in-situ microstructural observations brings direct constraints on the DRX mechanisms active during the different stages of the deformation. The evolution of the microstructure from the annealed state up to 12% strain is illustrated using successive in-situ KAM maps on sample X (Figure 6). Due to the pre-deformation annealing, the initial microstructure is characterized by smooth grain boundaries and a predominance of KAM values below 1°. Thus, if a GOS threshold is used, as in Figure 6, most grains are identified as recrystallized. However, the pre-deformation annealing did not suffice to produce a completely equilibrated microstructure. Apparent (2D) grain sizes are highly variable, ranging from a few to >100 μm and grain shapes are irregular, rather than polygonal. A few grains preserve scarce subgrain boundaries.

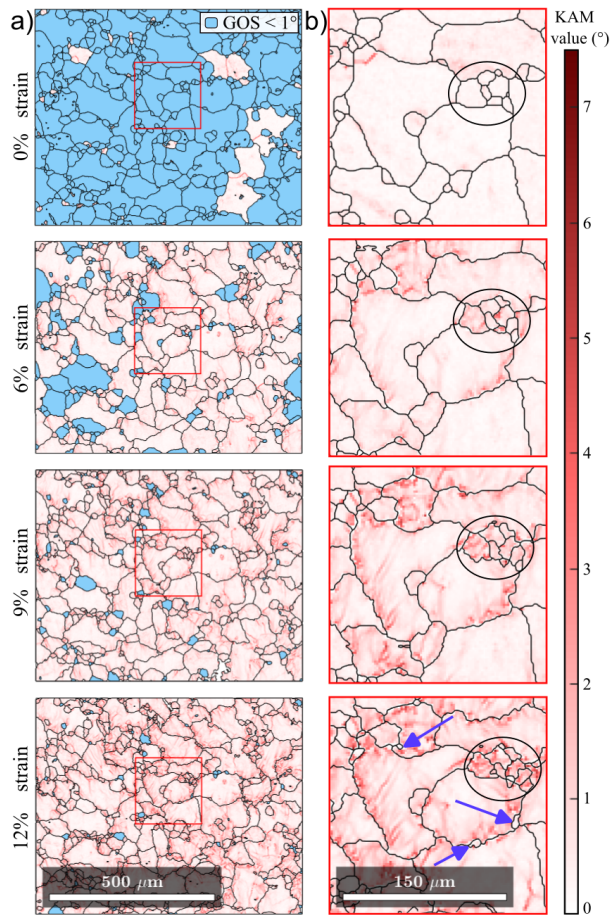


Figure 6. Microstructure evolution in the early stages of the experiments, illustrated by first order KAM maps obtained in situ at 0%, 6%, 9%, and 12% engineering strain for sample X. Grain boundaries, calculated using a 7.5° misorientation threshold, are represented as black lines. (a-d) Full size maps, in which the recrystallized grains identified using a 1° GOS threshold are coloured in blue. (e-f) Zoom on the area defined by the red square in (a-d); in the detail maps, KAM data for all grains are displayed, so that the evolution of the substructure within the DRX grains may also be visualized.

At 6% engineering strain, apparent grain sizes and grain shapes hardly evolved, but all grain boundaries became more serrated. Most grains developed significant intragranular misorientations, recorded as high KAM values, and the RX fraction based on the GOS, which was initially very high because of the pre-deformation annealing, is reduced to < 15%. Intragranular misorientation, documenting the accumulation of dislocations and formation of subgrain boundaries, is spatially heterogeneous, varying from grain to grain, but dislocation densities are systematically higher in the vicinity of grain boundaries (within < 10 μm of the boundary). Although very local, the first DRX events, characterized by reorganisation of the grain boundary structure, can already be documented at this early stage (cf. domains highlighted by an ellipse in Figure 6(b)). Grain boundaries migrated, leading to apparent (in 2D) formation or disappearance of grains. Some, but not all of these new grains, have GOS < 1°.

Misorientation maps at 9% and 12% engineering strain document a continuous progression of this microstructural evolution. Grain boundaries become increasingly more serrated. Intragranular misorientations are intensified and subgrains form in the vicinity of grain boundaries of most grains (Figure 6). Clear nucleation by bulging events is documented locally (blue arrows in Figure 6(b)). The strongest grain boundary reorganisation, with clear evidence for formation of new grains by DRX is, nevertheless, documented within the cluster of small grains (highlighted in Figure 6(b)), which already showed significant reorganization of the grain boundary microstructure at 9% engineering strain. Within this cluster, the microstructure is in continuous reorganisation, with concomitant polygonization (KAM values increase) and grain boundary migration producing increasingly serrated grain boundaries, bulging, and limited grain growth.

In summary, up to ~ 12% engineering strain, the evolution of the microstructure is dominated by a progressive accumulation of geometrically-necessary dislocations and their organisation into subgrain boundaries. Heterogeneous accumulation of dislocations in the close vicinity of grain boundaries triggers short-range migration, documented by increasing serration of the grain boundaries. DRX events, with nucleation by bulging assisted by subgrain rotation, remain very local.

In-situ microstructural data for the interval ~ 10% to ~ 23% engineering strain were perturbed by too short deformation steps (~ 2%) and significant recovery between EBSD acquisitions at 250°C, which explain faster grain growth and less serrated boundaries observed in sample C, and by drift during EBSD mapping for sample D. The in-situ EBSD maps for this interval are therefore not presented. Nevertheless, their analysis documents continued increase of the intragranular misorientation. It also highlights continuous grain boundary reorganisation and limited growth within isolated “clusters” of small grains, which progressively increase in area. These clusters have a higher than average density of grains with GOS < 1°, which may be clearly identified as newly formed DRX grains, but also contain small grains with high intragranular misorientations. The general shape of the initial coarse grains barely changes, despite a continuous increase in the serration of the grain boundaries, leading to local nucleation events by bulging assisted by subgrain rotation, and progressive increase in the misorientation across subgrain boundaries.

Analysis of the evolution of the microstructure between 23% and 38% engineering strain in Sample D documents continuation of the same evolution trend, with acceleration of the DRX between 33 and 38% engineering strain (Figure 7). DRX grains occur both as isolated small grains formed by bulging of the boundaries of the initial coarse grains and within clusters (outlined by black ellipses in Figure 7). The more strained is the sample, the more serrated become the grain boundaries. The progressive increase in misorientation across subgrain boundaries is well illustrated by the KAM maps, which depict the formation of complex subgrain boundary structures (left column in Figure 7). It is also documented by the intensification of the orientation contrasts in maps color-coded as a function of the axes accommodating the intragranular misorientations (center column in Figure 7) or as a function of the local angular misorientation relative to the

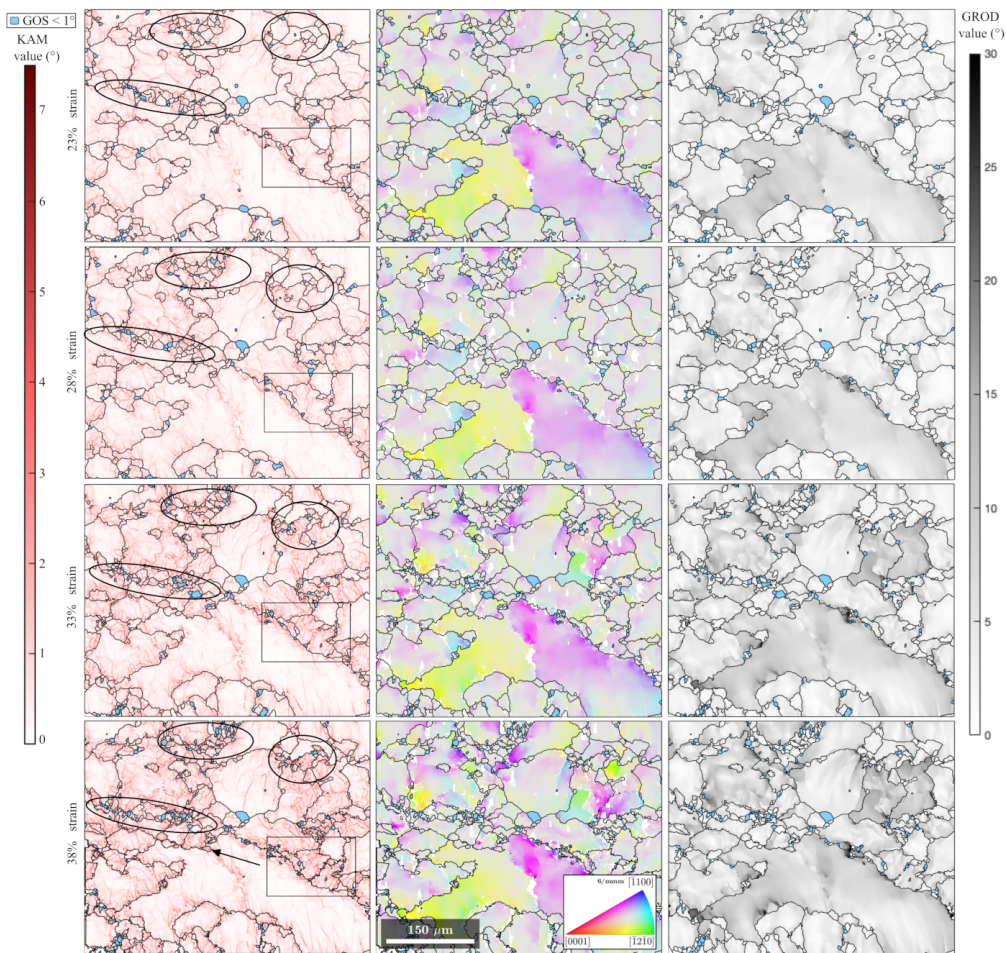


Figure 7. Microstructure evolution in the 23% to 38% strain interval, illustrated by in-situ first order KAM (left column), mis2mean maps (center column), and grain reference orientation deviation (GROD, right column) of sample D at 23%, 28%, 33%, and 38% engineering strain. Mis2mean maps display the misorientation axis relative to the mean grain orientation, GROD maps display the misorientation angle relative to the mean grain orientation. Grain boundaries calculated using a 7.5° misorientation threshold are represented as black lines. Recrystallized grains identified using a 1° GOS threshold are coloured in blue.

mean orientation of the grain (right column in Figure 7). This evolution is particularly clear in the coarse grain that occupies most of the lower part of the maps, which displays a strong orientation gradient accommodated by a 10-20 μm wide network of low-angle boundaries. This network becomes more complex and misoriented with increasing strain, but does not evolve into a well-defined grain boundary within the investigated strain interval. DRX is limited to its uppermost limit, where association of bulging and subgrain rotation produced a DRX grain (black arrow in the lower right panel of Figure 7), which already displayed, at its first observation, a well-developed substructure. Evolution of a similar network of low-angle boundaries into a seam of DRX grains is, nevertheless, recorded in a neighboring grain (highlighted by the rectangle in the KAM maps in Figure 7 and displayed in detail in Figure 8). The detail maps in Figure 8 also illus-

trate the acceleration of the DRX between 33 and 38% strain, documented by a net increase in the serration of the grain boundaries and an increase in the frequency of DRX events by both bulging and polygonization.

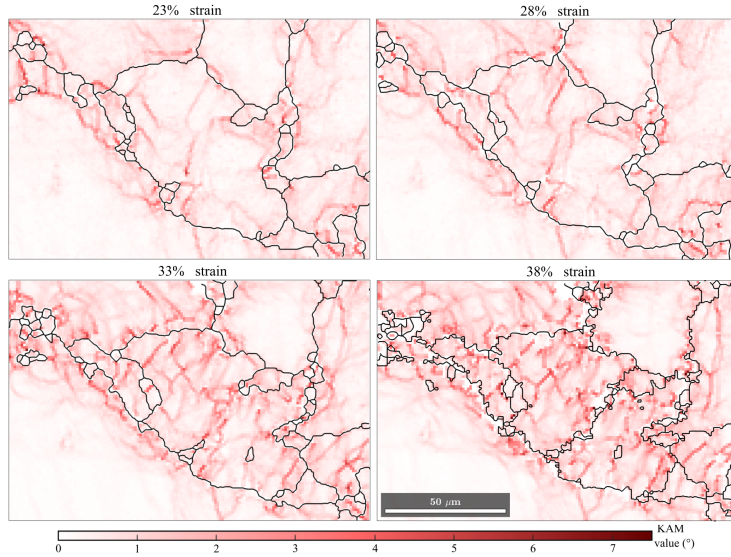


Figure 8. Zoom in the area delimited by a rectangle in Figure 7 illustrating the evolution of a network of low-angle boundaries into a seam of DRX grains as well as the acceleration of the bulging in the 33% to 38% strain interval relative to the preceding intervals. First order KAM maps of sample D at 23%, 28%, 33%, and 38% engineering strain. Grain boundaries calculated using a 7.5° misorientation threshold are represented as black lines.

As in the previous steps, the fastest microstructural evolution (higher number of nucleation and grain boundary migration events) is observed within the small-grain (DRX) clusters, which progressively increase in area (domains highlighted by ellipses in Figure 7). Yet, at 38% engineering strain, a continuous necklace of DRX grains is still not developed. Most of the boundaries of the initial coarse grains, despite their high serration, are free of DRX grains. This observation is consistent with the bulk measure of the RX area fraction defined based on a grain size threshold, which starts to increase in this strain interval (Figure 5(f)). In contrast, the RX fraction defined based on a GOS threshold remains almost constant (cf. area fraction of the grains highlighted in blue in Figure 7 and 5(e)). The discrepancy between the two measures may be partially explained by the contribution of polygonization (subgrain rotation) to DRX. This process is illustrated by the DRX grain highlighted by the arrow in Figure 7, in which the new grain boundaries, partially formed by polygonization, enclose preexisting substructure. This contrasts with nucleation by bulging, in which grain boundary migration cleans the dislocation substructure, producing DRX grains with little internal misorientation. Faster redeformation, leading to development of substructure within the DRX grains than grain growth, is another explanation for the lower DRX fraction estimated based on a GOS relative to that based on a grain size threshold.

The in-situ microstructural data for the interval $\sim 35\%$ to $\sim 47\%$ engineering strain in sample X documents a net progressive increase in the DRX fraction (Figure 9). The DRX clusters still display on average a faster microstructural evolution (higher number of nucleation and grain boundary migration events). However, DRX events become widespread, occurring along most grain boundaries and giving rise, at the end of this interval, to an almost continuous necklace of

small DRX grains (Figure 9(a)). The higher frequency of observations of bulging events (circles in Figure 9(b)) point to faster grain boundary migration relative to the previous strain intervals. Grain boundary migration rates and, hence the kinetics of nucleation, are nevertheless highly variable. The grain highlighted with a purple circle in Figure 9(b) formed progressively and, although a subgrain boundary developed in the necking region, it is still not fully separated from the parent grain at 44% strain. In contrast, the grain highlighted in green formed suddenly between 41% and 44% strain from a previously slowly migrating boundary. The in-situ EBSD observations for this strain range also highlight the discontinuous nature of the DRX processes at the grain scale. The zoom in Figure 9(c) documents the evolution of a DRX grain, which was tracked based on its position and crystallographic orientation. This DRX grain grew fast at the expenses of its highly deformed neighbors, from 35% to 41% strain, while maintaining its intragranular structure almost free of dislocation substructures. After that, grain growth slowed and dislocations started to accumulate, as documented by the build-up of a substructure with progressively increasing misorientation, and new DRX grains formed along its boundaries.

In situ EBSD data for the 47% to 67% strain interval provide similar observations to those of the 35% to \sim 47% strain interval. Progressive increase in the DRX fraction results in interconnection of the DRX clusters at strains $> 67\%$. This evolution is better documented in the large maps (Figure 4) than in the in-situ data.

3.4. Texture evolution

We quantify the texture evolution by: (1) the change in the angle between the normal to the $\langle c \rangle$ -axis girdle and the tension direction and (2) the intensity of the texture using a texture index proxy, the J-index (the integral of the squared orientation distribution function [34]). The initial texture is characterized by a girdle of $\langle c \rangle$ axis at $\sim 58^\circ$ to the tensile axis (Figure 10(c)), that is, an angle between the normal to the $\langle c \rangle$ -axis girdle and tensile axis, initially at $\sim 32^\circ$. With increasing strain, this angle decreases (Figure 10(a)). However, the texture reorientation rate progressively slows down and a quasi-steady orientation of the normal to the $\langle c \rangle$ -axis girdle at $\sim 20^\circ$ to the tensile axis is attained after 35% engineering strain. DRX grains (segmented based on the grain size) initially display similar, but more dispersed, orientations than the coarse grains, which control the bulk texture (Figure 10(d)) because they represent $>90\%$ of the mapped area. However, for engineering strains equal or higher than 35%, DRX grains have a texture characterized by a higher angle between the normal to the $\langle c \rangle$ -axis girdle and the tension axis ($\sim 24^\circ$ at strains $> 45\%$).

The measured textures intensity evolves slowly with increasing strain and even slightly decrease at the highest strains. An almost constant bulk J-index between 4 and 5.5 is obtained for the datasets obtained on large areas at the start or the end of the experiments (Figure 10(b)). Higher texture indexes are estimated based on the smaller maps collected in-situ during the experiments, but these data are biased by the presence of a few coarse grains that occupy large area fractions of these maps (cf. Figures 6 to 9). The DRX grains texture intensity, like many other quantities in the present experiments, changes around 35% engineering strain. Up to 35% strain, the DRX grains texture is only slightly more dispersed than the bulk texture. The DRX grains texture dispersion increases between 30% - 40% strain and then stabilizes at texture indexes between 2 and 2.5.

The bulk texture evolution documented in the present experiments deviates from that predicted by a VPSC simulation with no DRX and slip systems' data adapted to simulate deformation of AZ31 at 250°C and moderate strain rates (see Section 2.5). This VPSC simulation predicts continuous, though at a progressively decreasing rate, concentration and rotation of the texture towards parallelism between the normal to the $\langle c \rangle$ axis girdle and the tension axis (continuous lines in Figures 10(a) and (b)). The bulk experimental textures displays a slower rotation of the

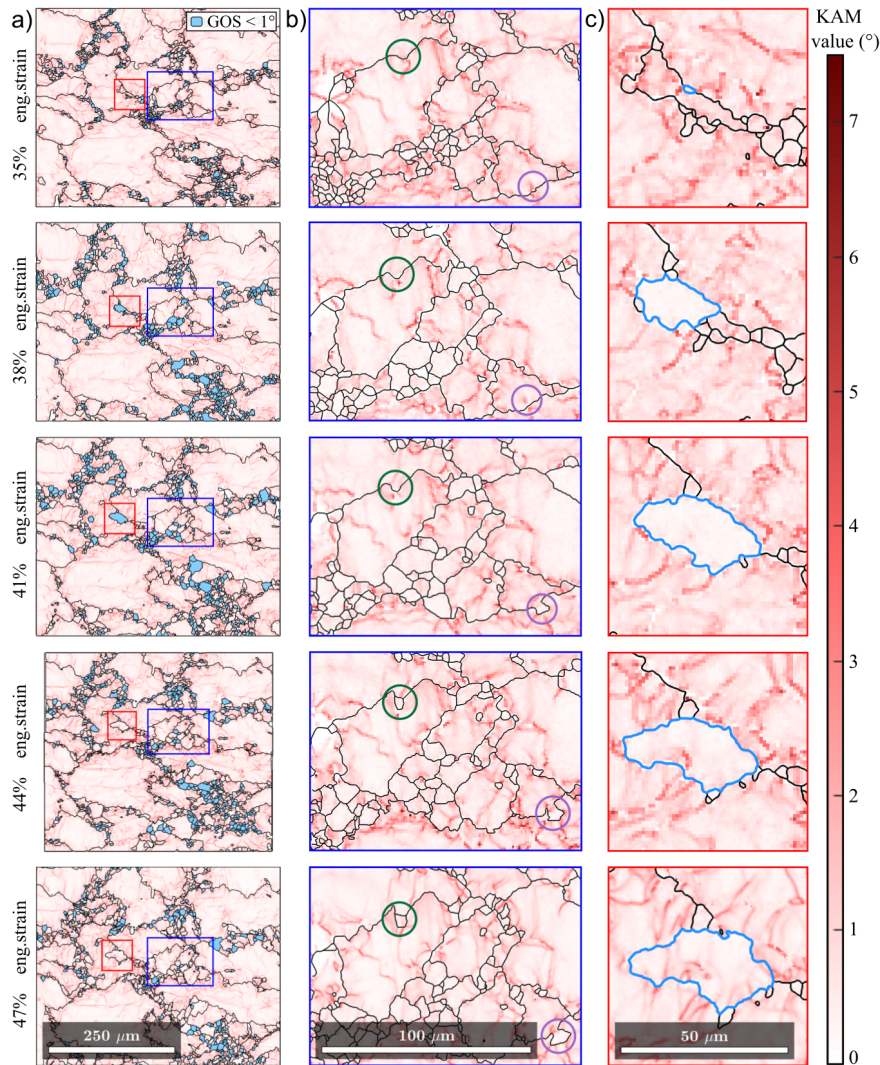


Figure 9. Microstructure evolution between 35% and 47% engineering strain illustrated by KAM maps obtained *in situ* for sample X at 35%, 38%, 41%, 44%, and 47% engineering strain. All maps but that at 47% strain were acquired with a 1 μm step size; the map at 47% strain was acquired with a step size of 0.5 μm . To keep absolute KAM values comparable over the entire strain range, the KAM order has been adjusted: first order KAM data is presented for all maps except for that at 47% strain, which displays second order KAM data. Grain boundaries calculated using a 7.5° misorientation threshold are represented by black lines. (a) Full size maps, in which recrystallized grains identified using a 1° GOS threshold are coloured in blue. (b) Zoom on the area defined by the blue rectangle in (a); dark green and purple circles are used to highlight areas showing nucleation events. (c) Zoom on the area defined by the red rectangle in (a), which displays the growth and re-accumulation of local misorientation in a recrystallized grain (highlighted in light blue) that is tracked using its location and crystallographic orientation from map to map.

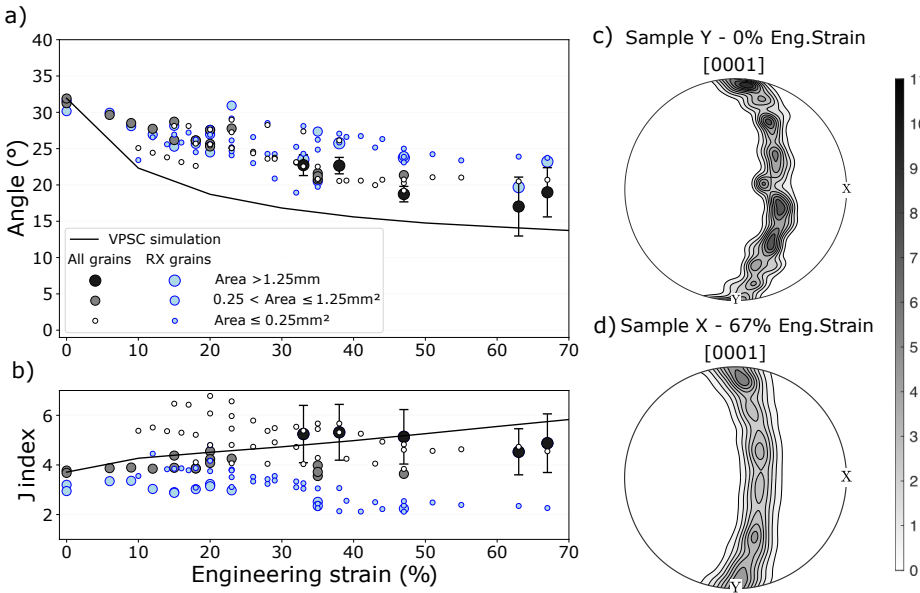


Figure 10. Evolution of the texture with increasing engineering strain: (a) orientation of the texture, defined by the angle between the normal to the $\langle c \rangle$ axis girdle and the tension direction and (b) texture strength, defined by the J-index. Symbols in white, gray, and black correspond to full orientation data (bulk texture), considering one orientation per pixel. Coarser symbols and darker colors mark data from larger, post-mortem maps. To estimate the spatial variability of the data and the representativity of the smaller in-situ maps, the large maps ($\text{area} > 1.25 \text{ mm}^2$) have been re-sampled as multiple smaller maps with areas similar to that of the in-situ ones ($\sim 0.2 \text{ mm}^2$) to derive the mean and the standard deviation, represented by the error bars, of the distributions. For comparison, the texture of the recrystallized fraction identified using a $20 \mu\text{m}$ threshold in each map is represented by blue symbols; as for the full orientation data, the symbol sizes are proportional to the area of the map. The continuous solid lines indicate the texture evolution predicted for a monotonic axial tension experiment by a 2nd order VPSC simulation without DRX (see Section 2.4) in which the initial texture is that of the starting material. The parameters used in the VPSC simulation are defined in the methods section. (c) and (d) Pole figures presenting the initial texture (sample Y) and the final texture measured at 67% engineering strain (sample X); colourscale and contours in multiples of a uniform distribution.

normal to the $\langle c \rangle$ axis girdle towards the tension direction. The rotation of the texture is even slower for the RX grains, which tend to display a stable orientation of the normal to the $\langle c \rangle$ axis girdle at ca. 25° to the tension direction for all strains $> 35\%$. The concentration of the bulk textures with increasing strain follows the VPSC predictions up to 47% engineering strain, but stabilizes thereafter. At all strains, the DRX grains texture is weaker than both the measured bulk texture and the VPSC predictions. Thus, DRX slows down both the concentration and reorientation of the texture. Better adjustment of the experimentally observed texture evolution is obtained for VPSC simulations with a lower viscoplastic anisotropy (cf. Supplementary Material). However, such a low contrast between the CRSS of the basal and prismatic or pyramidal systems (factor 4) is only expected at significantly higher temperatures ($>350^\circ\text{C}$) [13, 33] than that of the present experiments.

4. Discussion

As already observed by many others (e.g. [14, 18, 19, 35]), for the temperature and strain-rate conditions considered in the present study, AZ31 undergoes continuous DRX. This process involves three steps: first, accumulation and rearrangement of dislocations into low-angle boundaries, that is, polygonization (see Figures 6 and 7); second, formation of new grains (see Figure 9) by both subgrain rotation (progressive increase in the misorientation of a low-angle boundary by absorption of dislocations - see Figure 9(b)) and bulging (short-range grain boundary migration controlled by local variations in dislocation densities in the vicinity of the grain boundaries). Nucleation may be followed by limited grain growth, in contrast to discontinuous DRX where grain growth is a major mechanism. Most newly formed DRX grains have low dislocation densities, denoting the important role of bulging, which allows for removal of dislocations by migrating boundaries, in the nucleation (see Figure 9(c)). However, these grains eventually accumulate dislocations and recrystallize again (Figure 9(c)). In addition, in-situ observations show that polygonization may result in DRX nuclei with significant substructure (DRX grain highlighted by the arrow in Figure 7(b)). Finally, even when nucleation is dominated by bulging, the bulges are most often closed by subgrain boundaries that evolve into grain boundaries (Figures 6 and 9(b)).

The in-situ observations document that DRX starts at strains as low as 9 % (cf. highlighted domain in Figure 6(b)), evolves slowly until $\sim 35\%$ engineering strain, and accelerates thereafter (cf Figures 7 and 9). Up to 35% strain, the microstructural evolution is dominated by substructure formation and thereafter by nucleation and limited grain growth. These observations are corroborated by statistical analysis of the entire microstructural dataset: all parameters show a change in trend around 35% engineering strain (Figure 5). KAM and subgrain boundary density data document that substructure formation is more active, with progressive increase in the intragranular misorientation before this threshold and remains nearly constant after. In contrast, the grain boundary density and DRX fraction evolve little before 35% strain and increase steadily thereafter. The acceleration of nucleation is also recorded by a net decrease in grain size. The present microstructural observations point therefore to a threshold in the microstructure evolution by DRX, with an acceleration of the grain boundary migration rates at strains $> 35\%$. This allows for a progressive transition, at higher strains, from DRX localized in isolated clusters towards a state in which DRX progressively spreads over the sample, with interlinkage of the DRX clusters producing a necklace-type microstructure.

However, the sharp change in the microstructural evolution and acceleration of DRX at $\sim 35\%$ engineering strain is not accompanied by acceleration in the strain softening. The mechanical curves for all samples show a marked decrease in the work hardening rate at 10-15% engineering strain, followed by a constantly decreasing hardening rate, which leads to a smooth transition from hardening to softening at $\sim 30\%$ engineering strain (Figure 2). Accelerated softening is only observed for engineering strains $> 60\%$.

The present microstructural observations are also at odds with determination of the critical strain for onset of DRX from flow curves using the second derivative method of Poliak and Jonas [36] ([4] ; [24]). For the present experiments, this method predicts onset of DRX at an engineering strain of 18% (Figure 2(b)). However, the in-situ microstructural observations document that DRX started at engineering strains as low as 9 % (cf. highlighted domain in Figure 6(b)) and display no evidence for a change in the DRX kinetics at engineering strains of 18%.

The present flow curves are, nevertheless, consistent in shape with previous data for tensile tests on AZ31 at 200°C [26], even if the transition between hardening and softening and the failure occurred at lower strains in the previous experiments. Tam et al. [26] succeeded to reproduce their experimental flow curves by a DRX-VPSC model, which included nucleation and

twinning. In this model, onset of DRX depends on a critical dislocation density and the newly formed DRX grains have very low dislocation density and random disorientation relative to the parent grains. The assumption of a dislocation density threshold is consistent with the present microstructural observations. Tam et al. [26] simulations predicted, however, significantly higher DRX fractions ($\sim 40\%$ at 35% strain for loading parallel oblique to the $\langle c \rangle$ -axis maximum of the initial texture) than those observed in the present experiments. A possible explanation would be an underestimation of the geometrical softening due to DRX in Tam et al. [26] simulations, which did not perfectly reproduce the measured textures.

In the present study, we adopt a simpler strategy to discriminate between the contributions to softening of DRX-induced changes in texture from DRX-induced changes in the dislocation density, which result in DRX grains more compliant than the deformed parent grains. We compare the stresses predicted by one-step VPSC simulations, performed with the same parameters as the monotonic axial tension VPSC simulation displayed in Figure 10, but using as initial texture the experimental textures measured at different strains to the stresses predicted for the monotonic axial tension VPSC simulation with as the initial texture that of the starting experimental material. As hardening is not considered in these VPSC simulations, the difference in stress predictions results solely from the difference between the measured and simulated textures at each strain. This comparison (Figure 11) shows that the DRX-induced changes in texture counteracts most of the geometrical hardening predicted for a texture evolution due to dislocation glide. This lower geometrical hardening results from a more compliant orientation of the DRX grains, but also from the slower rotation of the parent grains compared with the expected rotation with no recrystallization (Figure 10). The slower texture evolution in the experiments starts at strains as low as 6%. This suggests that polygonization may effectively slow down the texture evolution and produce thereby significantly bulk softening.

VPSC simulations with lower viscoplastic anisotropy, presented in the Supplementary Material, show almost no difference between the stresses predicted for a monotonic axial tension experiments and those calculated using the experimental textures at various strains, because lower viscoplastic anisotropy results geometrical hardening. These simulations also better reproduce the experimental textures. As stated in the previous section, such a low viscoplastic anisotropy should only prevail at much higher temperatures ($>350^\circ\text{C}$) than those of the present experiments [13, 33]. However, the better adjustment of the experimental data by these simulations hints for the role of DRX on resolving viscoplastic strain incompatibilities that arise between differently oriented grains in highly anisotropic polycrystals.

Microstructural softening, due to the lower initial dislocation density in the DRX grains and, maybe, also to the increase in the grain boundary area, which may favor grain boundary-assisted deformation mechanisms, is nevertheless required to compensate for hardening due to the increase in the dislocation density in the initial states and this contribution has to increase to explain the effective softening observed at strains $> 35\%$. The discrepancy between the acceleration of the microstructural changes observed in both the in-situ data and statistics of the entire dataset at 35% strain and the continuous evolution of the mechanical behavior implies, however, that the bulk softening does not depend solely on the DRX volume fraction, but also on its spatial organization. To explain these observations, we hypothesize that isolated clusters of DRX have a limited effect on the bulk mechanical behavior, mainly avoiding stress peaks associated with local viscoplastic strain incompatibility. Homogenization of the stresses within the sample by DRX may explain tensile deformation to high strains without necking. Progressive interconnection of the DRX clusters results in progressively increasing bulk softening. Full interconnection, that is, development of a throughgoing necklace structure of DRX grains at the sample scale leads to major softening and, in a tensional test, drastic strain localization (Figure 3).

Onset of DRX after a critical strain paired with a single peak mechanical behavior are charac-

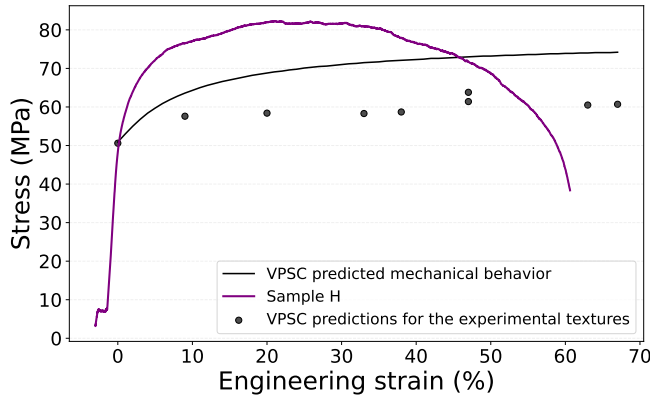


Figure 11. Comparison between the mechanical behavior predicted using a 2nd order VPSC model without DRX for : (1) a monotonic uniaxial tension experimental with as the initial texture that of the starting experimental material (full black line) and (2) one-step simulations with as the initial texture those measured post-mortem at different finite strains (dots). The difference between the two values is an estimate of the geometrical (texture-induced) hardening. The mechanical data for sample H is presented for comparison. The simulations predict correctly the stresses at the onset of the viscoplastic deformation, but the simulated and measured curves diverge fast, because intrinsic (dislocation-related) hardening or softening are not considered in the VPSC simulations. The parameters used in the VPSC simulations are defined in the methods section. Results for VPSC simulations using other parameters are presented in the Supplementary Material.

teristic of DRX producing a necklace-type structure [37]. This behavior is expected for ratios of D_0 the initial grain size over D_S the recrystallized grain size > 2 [4, 17], a condition fulfilled in the present experiments. However, the evolution of the DRX microstructure observed in the present study departs significantly from the schematic model of necklace formation, in which DRX propagates layer by layer from the boundaries towards the center of the parent grains [3, 4, 25, 38]. Our in-situ observations document a more complex evolution. DRX starts in multiple isolated small-grain clusters composed by grains w up to 35% strain most of the DRX takes place within those clusters rather than propagating into the coarse grains (Figures 4, 9). The high viscoplastic anisotropy of Mg AZ31 certainly favors a spatially heterogeneous onset of DRX and the higher density of grain boundaries within the clusters may favor recrystallization within them, as it will favor the formation of dislocation pile-ups [39] and, by consequence, nucleation. Even at strains $> 35\%$, increase in the DRX fraction results mainly in lateral extension and interconnection of the clusters, producing a necklace structure composed of a network of fine grained bands with irregular shapes, dominantly oriented at 25 to 45° to the tension direction. Drastic weakening related to interconnection of the DRX network at the sample scale results, in the present tensile tests, in ductile rupture well before full recrystallization of the sample (maximum DRX fraction $< 35\%$). This maximum DRX fraction is consistent with previous results for AZ31 deformed in tension at similar temperature and strain rate conditions [18].

5. Conclusions

We conducted tensile tests on AZ31 samples with in-situ EBSD acquisition at 250°C and 10^{-3} s⁻¹ to characterize the evolution of dynamic recrystallization (DRX) and its effect on the mechanical

behavior. EBSD mapping allows monitoring the evolution of the DRX process at both local and bulk (sample) scales. Despite the complexity and local nature of the DRX mechanisms, the microstructural dataset and mechanical data acquired on multiple specimens over the entire deformation range up to failure at 65-67% engineering strain is remarkably coherent.

In-situ microstructural observations show onset of CDRX at strains as low as 9%, with nucleation occurring by an association of subgrain rotation and bulging and very limited grain growth. Both in-situ microstructural observations and statistical analysis of the evolution of KAM, subgrain and grain boundary densities, grain sizes, and DRX fraction document a long incubation period, up to 35% strain, which is dominated by dislocation accumulation and reorganization (polygonization). During this stage, DRX is limited to isolated small-grain clusters, which display fast microstructural evolution, but limited growth. This is followed by an acceleration of the DRX process recorded by widespread, but spatially heterogeneously distributed grain nucleation and growth. At the studied experimental conditions, grain growth is slow relative to nucleation and build-up of dislocation substructures, producing a marked average grain size reduction. Increase in the DRX fraction results therefore in formation of a continuous RX-necklace microstructure. The in-situ data also highlights the local discontinuous nature of DRX with nucleation by coupled bulging and subgrain rotation (polygonization), followed by grain growth and re-accumulation of dislocation substructures. Averaging of these local processes over the sample volume produces a continuous evolution.

All experiments show a consistent mechanical behavior characterized by a marked decrease in the hardening rate at 10-15% engineering strain, followed by a constantly decreasing hardening rate, which leads to a continuous transition from hardening to softening at $\sim 30\%$ engineering strain, and an accelerated softening leading to ductile failure at engineering strains $> 60\%$. The sharp change in the microstructural evolution and acceleration of DRX at $\sim 35\%$ engineering strain is never accompanied by acceleration in the strain softening.

A comparison between the textural observations and predictions by VPSC simulations without DRX shows that DRX slows down the texture evolution, counteracting most of the geometrical hardening produced in tension by texture evolution in response to dislocation glide. Microstructural softening is, nevertheless, required to compensate hardening due to the increase in the dislocation density. Moreover, the intensity of microstructural softening has to increase with strain to explain the steadily decreasing hardening rate between 15% and $\sim 60\%$ engineering strain. The discrepancy between the kinetics of the microstructural evolution and the mechanical behavior implies, however, that the bulk softening does not depend solely on the DRX volume fraction, but also on its spatial organization. To explain these observations, we hypothesize that isolated clusters of DRX have a limited effect of the bulk mechanical behavior, mainly avoiding stress peaks associated with local viscoplastic strain incompatibility. Homogenization of the stresses within the sample by DRX may account for the observed tensile deformation to high strains without necking. Progressive interconnection of the DRX clusters results in progressively increasing bulk softening. Development of a throughgoing necklace structure of DRX grains at the sample scale leads to major softening, which results, in the present tensional test, in drastic strain localization.

Conflicts of interest

The authors declare no competing financial interest.

Dedication

The manuscript was written through contributions of all authors. All authors have given approval to the final version of the manuscript.

Acknowledgments

We are grateful to Christophe Nevado from Géosciences Montpellier for his support in the preparation of the samples. We thank Thomas Chauve for fruitful discussions.

Supplementary data

Supporting information for this article is available on the journal's website under article's URL or from the author.

Declaration of interests

The authors do not work for, advise, own shares in, or receive funds from any organization that could benefit from this article, and have declared no affiliations other than their research organizations.

References

- [1] T. Sakai, A. Belyakov, R. Kaibyshev, H. Miura and J. J. Jonas, "Dynamic and Post-Dynamic Recrystallization under Hot, Cold and Severe Plastic Deformation Conditions", *Prog. Mater. Sci.* **60** (2014), pp. 130–207.
- [2] J. Humphreys, G. S. Rohrer and A. Rollett, *Recrystallization and Related Annealing Phenomena*, Elsevier, 2017.
- [3] H. K. Zhang, H. Xiao, X. W. Fang, Q. Zhang, R. E. Logé and K. Huang, "A Critical Assessment of Experimental Investigation of Dynamic Recrystallization of Metallic Materials", *Mater. Des.* **193** (2020), article no. 108873.
- [4] H. Mirzadeh, "Grain Refinement of Magnesium Alloys by Dynamic Recrystallization (DRX): A Review", *J. Mater. Res. Technol.* **25** (2023), pp. 7050–7077.
- [5] Q. Ma, B. Li, W. R. Whittington, A. L. Oppedal, P. T. Wang and M. F. Horstemeyer, "Texture Evolution during Dynamic Recrystallization in a Magnesium Alloy at 450°C", *Acta Mater.* **67** (2014), pp. 102–115.
- [6] B. L. Mordike and T. Ebert, "Magnesium: Properties —applications —potential", *Mater. Sci. Eng. A* **302** (2001), no. 1, pp. 37–45.
- [7] J. Hirsch and T. Al-Samman, "Superior light metals by texture engineering: Optimized aluminum and magnesium alloys for automotive applications", *Acta Mater.* **61** (2013), no. 3, pp. 818–843.
- [8] M. Montagnat, T. Chauve, F. Barou, A. Tommasi, B. Beausir and C. Pressengeas, "Analysis of Dynamic Recrystallization of Ice from EBSD Orientation Mapping", *Front. Earth Sci.* **3** (2015).
- [9] T. Chauve, M. Montagnat, F. Barou, K. Hidas, A. Tommasi and D. Mainprice, "Investigation of Nucleation Processes during Dynamic Recrystallization of Ice Using Cryo-EBSD", *Philos. Trans. R. Soc. Lond., Ser. A* **375** (2017), no. 2086, article no. 20150345.
- [10] S. Fan, T. F. Hager, D. J. Prior, A. J. Cross, D. L. Goldsby, C. Qi, M. Negrini and J. Wheeler, "Temperature and strain controls on ice deformation mechanisms: insights from the microstructures of samples deformed to progressively higher strains at -10, -20 and -30, °C", *Cryosphere* **14** (2020), no. 11, pp. 3875–3905.
- [11] J. L. Urai, C. J. Spiers, H. J. Zwart and G. S. Lister, "Weakening of Rock Salt by Water during Long-Term Creep", *Nature* **324** (1986), no. 6097, pp. 554–557.
- [12] M. A. Lopez-Sanchez, A. Tommasi, W. Ben Ismail and F. Barou, "Dynamic Recrystallization by Subgrain Rotation in Olivine Revealed by Electron Backscatter Diffraction", *Tectonophysics* **815** (2021), article no. 228916.
- [13] F. Zhang, M. Sun, B. Sun, F. Zhang, Y. Bai and Z. Liu, "Temperature Dependency on the Microscopic Mechanism in the Normal Direction of Wrought AZ31 Sheet under Dynamic Compressive Behavior", *Materials* **14** (2021), no. 23, article no. 7436.
- [14] T. Al-Samman and G. Gottstein, "Dynamic Recrystallization during High Temperature Deformation of Magnesium", *Mater. Sci. Eng. A* **490** (2008), no. 1-2, pp. 411–420.
- [15] T. Al-Samman and G. Gottstein, "Room Temperature Formability of a Magnesium AZ31 Alloy: Examining the Role of Texture on the Deformation Mechanisms", *Mater. Sci. Eng. A* **488** (2008), no. 1-2, pp. 406–414.
- [16] C. D. Barrett, A. Imandoust, A. L. Oppedal, K. Inal, M. A. Tschopp and H. El Kadiri, "Effect of Grain Boundaries on Texture Formation during Dynamic Recrystallization of Magnesium Alloys", *Acta Mater.* **128** (2017), pp. 270–283.
- [17] S. M. Fatemi-Varzaneh, A. Zarei-Hanzaki and H. Beladi, "Dynamic Recrystallization in AZ31 Magnesium Alloy", *Mater. Sci. Eng. A* **456** (2007), no. 1-2, pp. 52–57.

- [18] J. C. Tan and M. J. Tan, "Dynamic continuous recrystallization characteristics in two stage deformation of Mg–3Al–1Zn alloy sheet", *Mater. Sci. Eng. A* **339** (2003), no. 1-2, pp. 124–132.
- [19] X. Yang, H. Miura and T. Sakai, "Dynamic Evolution of New Grains in Magnesium Alloy AZ31 during Hot Deformation", *Mater. Trans.* **44** (2003), no. 1, pp. 197–203.
- [20] M. R. Barnett, A. G. Beer, D. Atwell and A. Oudin, "Influence of Grain Size on Hot Working Stresses and Microstructures in Mg–3Al–1Zn", *Scr. Mater.* **51** (2004), no. 1, pp. 19–24.
- [21] N. V. Dudamell, I. Ulacía, F. Gálvez, et al., "Influence of Texture on the Recrystallization Mechanisms in an AZ31 Mg Sheet Alloy at Dynamic Rates", *Mater. Sci. Eng. A* **532** (2012), pp. 528–535.
- [22] M. R. Barnett, "Quenched and Annealed Microstructures of Hot Worked Magnesium AZ31", *Mater. Trans.* **44** (2003), no. 4, pp. 571–577.
- [23] A. G. Beer and M. R. Barnett, "Microstructural Development during Hot Working of Mg-3Al-1Zn", *Metall. Mater. Trans. A* **38** (2007), no. 8, pp. 1856–1867.
- [24] X. Liu, J. J. Jonas, L. X. Li and B. W. Zhu, "Flow Softening, Twinning and Dynamic Recrystallization in AZ31 Magnesium", *Mater. Sci. Eng. A* **583** (2013), pp. 242–253.
- [25] D. Ponge and G. Gottstein, "Necklace Formation during Dynamic Recrystallization: Mechanisms and Impact on Flow Behavior", *Acta Mater.* **46** (1998), no. 1, pp. 69–80.
- [26] K. J. Tam, M. W. Vaughan, L. Shen, M. Knezevic, I. Karaman and G. Proust, "Modelling Dynamic Recrystallisation in Magnesium Alloy AZ31", *Int. J. Plast.* **142** (2021), article no. 102995.
- [27] H. Mirzadeh, "Constitutive Analysis of Mg–Al–Zn Magnesium Alloys during Hot Deformation", *Mech. Mater.* **77** (2014), pp. 80–85.
- [28] M.-S. Chen, W.-Q. Yuan, H.-B. Li and Z.-H. Zou, "New Insights on the Relationship between Flow Stress Softening and Dynamic Recrystallization Behavior of Magnesium Alloy AZ31B", *Mater. Charact.* **147** (2019), pp. 173–183.
- [29] R. A. Lebensohn and C. N. Tomé, "A self-consistent anisotropic approach for the simulation of plastic deformation and texture development of polycrystals: Application to zirconium alloys", *Acta Metall. Mater.* **41** (1993), no. 9, pp. 2611–2624.
- [30] C. N. Tomé and R. A. Lebensohn, *Manual for Code – Visco-Plastic Self Consistent (VPSC) – Version 7c*, 2009. <https://fr.scribd.com/document/236442768/VPSC7c-Manual>.
- [31] R. A. Lebensohn, P. P. Castañeda, R. Brenner and O. Castelnau, "Full-Field vs. Homogenization Methods to Predict Microstructure–Property Relations for Polycrystalline Materials", in *Computational Methods for Microstructure–Property Relationships* (S. Ghosh and D. Dimiduk, eds.), Springer, 2011, pp. 393–441.
- [32] G. Zhou, M. K. Jain, P. Wu, Y. Shao, D. Li and Y. Peng, "Experiment and Crystal Plasticity Analysis on Plastic Deformation of AZ31B Mg Alloy Sheet under Intermediate Temperatures: How Deformation Mechanisms Evolve", *Int. J. Plast.* **79** (2016), pp. 19–47.
- [33] A. Chapuis and Q. Liu, "Investigating the Temperature Dependency of Plastic Deformation in a Mg–3Al–1Zn Alloy", *Mater. Sci. Eng. A* **725** (2018), pp. 108–118.
- [34] H.-J. Bunge, *Texture Analysis in Materials Science*, Butterworths & Co, 1982.
- [35] S. E. Ion, F. J. Humphreys and S. H. White, "Dynamic Recrystallisation and the Development of Microstructure during the High Temperature Deformation of Magnesium", *Acta Metall.* **30** (1982), no. 10, pp. 1909–1919.
- [36] E. I. Poliak and J. J. Jonas, "A One-Parameter Approach to Determining the Critical Conditions for the Initiation of Dynamic Recrystallization", *Acta Mater.* **44** (1996), no. 1, pp. 127–136.
- [37] C. Rehrl, S. Kleber, O. Renk and R. Pippan, "Effect of Forming Conditions on the Softening Behavior in Coarse Grained Structures", *Mater. Sci. Eng. A* **528** (2011), no. 19–20, pp. 6163–6172.
- [38] F. J. Humphreys and M. Hatherly, *Recrystallization and Related Annealing Phenomena*, Elsevier, 2012.
- [39] P. Duval, F. Louchet, J. Weiss and M. Montagnat, "On the Role of Long-Range Internal Stresses on Grain Nucleation during Dynamic Discontinuous Recrystallization", *Mater. Sci. Eng. A* **546** (2012), pp. 207–211.